Geophys. J. R. astr. Soc. (1973) **34**, 149–177.

Critically Refracted Waves in a Spherically Symmetric Radially Heterogeneous Earth Model

David P. Hill

(Received 1973 April 23)*

Summary

A theoretical analysis of acoustic waves refracted by a spherical boundary across which velocity and density increase abruptly and below which velocity and density may either increase or decrease continuously with depth is formulated in terms of waves generated at a harmonic point source and scattered by a radially heterogeneous spherical body. Through the application of an Earth-flattening transformation on the radial solution and the Watson transform on the sum over eigenfunctions, the solution to the spherical problem for high frequencies is expressed as an integral for the corresponding half-space problem in which the effect of boundary curvature maps into an effective positive velocity gradient with depth. The results of both analytical and numerical evaluation of this integral can be summarized as follows for body waves in the crust and upper mantle:

(1) In the special case of a critical velocity gradient (a gradient equal and opposite to the effective curvature gradient), waves interacting with the boundary at the critical angle of incidence have the same form as the classical head wave for flat, homogeneous layers.

(2) For gradients more negative than critical, the amplitude of waves incident at the critical angle decay more rapidly with distance than the classical head wave.

(3) For gradients that are positive, null, and less negative than critical, the amplitude of waves near the critical angle decays less rapidly with distance than the classical head wave, and at sufficiently large distances, the refracted wave field can be adequately described in terms of ray-theoretical diving waves. At intermediate distances from the critical point, the spectral amplitude of the refracted wave is scalloped due to multiple diving wave interference.

1. Introduction

This paper describes the wave-theoretical nature of energy that is generated at a point source and critically refracted or nearly critically refracted by an abrupt

* Received in original form 1972 December 6.

increase in velocity in a spherically symmetric, radially heterogeneous body. Seismic waves in the Earth associated with such energy are commonly the first arrivals recorded on seismograms out to distance of 1000 km or more from the source. They form the well-known P_g and P_n branches on local travel-time curves and represent the primary data of classical seismic–refraction studies. Much that is known about the best established and most widely recognized structures in the outer 200 km of the Earth (e.g. the 'granitic layer' in the continental crust or the Mohorovicic discontinuity at the base of the crust) is based on the travel times of these phases using geometrical ray theory. Because ray theory fails to predict the amplitude or wave form associated with critically refracted energy, however, a wave theory is necessary if these waves are to be used to further refine details of the major structural units of the crust and upper mantle in terms of velocity gradients, transition zones, and anelasticity.

Theoretical methods for treating critically refracted waves, or head waves from a plane boundary between two homogeneous media are well established (Brekhovskikh 1960; Cagniard 1962; Cerveny 1965; de Hoop 1960) and have been extended to include reflected and refracted waves in a arbitrary number of plane, homogeneous layers (Berry & West 1966; Fuchs 1968; Helmberger 1968; Müller 1970). Through Earth-flattening approximation, these methods have been generalized to include the effects of curvature for outer layers in Earth models (Gilbert & Helmberger 1971; Müller 1971). Cerveny & Ravindra (1971) provide a systematic treatment of the high-frequency properties of head waves based on asymptotic ray theory together with a fairly complete summary of the pertinent literature.

A limited number of exact solutions have been obtained for waves reflected in plane media with continuous variations in material properties with depth (Brekhovskikh 1960). Chekin (1964, 1965) has investigated some of the high-frequency, asymptotic effects of small velocity gradients on head wave propagation at a plane boundary; although, as Richards (1971) has pointed out, Chekin (1964) did not choose the proper potential representation for $P-SV$ motion in a vertically heterogeneous elastic medium. Some of the effects of small positive velocity gradients on acoustic head waves have been summarized by Cerveny (1966) and Cerveny & Jansky (1967) based primarily on the basis of Chekin's (1965) results for acoustic waves and ray theory. The effects of transition zones on reflected and refracted waves have been studied by Nakamura (1964), Hirasawa & Berry (1971), and Merzer (1971).

Mathematical methods such as the Watson transform and rainbow expansion (Bremmer 1937; Scholte 1956) have been used in seismology primarily to study the diffraction of body waves by the core–mantle boundary in spherically symmetric Earth models. See Chapman & Phinney (1972) for a recent summary. Buldryev and Lanin, however, have taken this approach to investigate 'interference waves' generated by waves incident on homogeneous cylinders and spheres (Buldyrev 1964; Buldyrev & Lanin 1966a, b; Lanin 1968). These 'interference waves' are closely related to the head wave in plane, homogeneous layers.

In this paper we consider waves from a point source interacting with a spherical boundary in terms of a steady-state boundary-value problem. To emphasize the principal aspects of the wave field with a minimum of algebra, we will consider acoustic waves in fluid media. The basic problem is similar to that treated by Buldyrev & Lanin (1966b) and Lanin (1968) for a homogeneous sphere, although in this paper an inhomogeneous sphere is considered and the results are expressed in a form more readily interpreted in terms of seismological applications. The analysis in this paper differs from Buldyrev & Lanin's treatment of the homogeneous sphere in that an Earth-flattening transformation is used, which puts the final integrals in a form similar to those used by Chekin (1964, 1965) to study an inhomogeneous half-space.

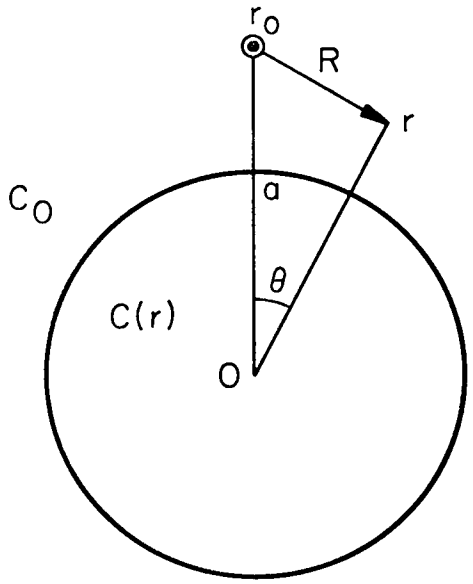

FIG. 1. Co-ordinate system for a spherically symmetric medium with a discontinuous boundary at $r = a$ between a homogeneous region (c_0) and a radially heterogeneous region ($c(r)$). The point source and receiver are located at r_0 and r, respectively.

2. General formulation

Consider the model illustrated in Fig. 1 in which waves generated by a point source at $(r_0, 0)$ are scattered by a spherical body of radius $r = a$ $(a < r_0)$ within which the material properties may be radially heterogeneous, and the acoustic velocity at the surface of the body is greater than in the surrounding homogeneous space. This corresponds to the geophysical problem of a source in a homogeneous layer over a first-order discontinuity in velocity at $r = a$, below which the velocity may vary smoothly with depth. In this treatment, however, the effects of layering and the free surface above the source are neglected.

Using an acoustic pressure potential of the form

$$\Phi = \frac{P}{\sqrt{d}}, \tag{1}$$

where P is the deviation from static ambient pressure and d is density, the Fourier transformed acoustic equations of motion for radially heterogeneous media reduce to a Helmholtz equation, or

$$\nabla^2 \Phi(\mathbf{r}) + [k(r)]^2 \Phi(\mathbf{r}) = 0 \tag{2}$$

under the condition that

$$|k|^2 \gg \left| \frac{1}{2d} \nabla^2 d - \frac{3}{4} \left(\frac{\nabla d}{d} \right)^2 \right|$$

(Brekhovskikh 1960). The general solution to the Helmholtz equations and boundary conditions for the wave field generated by a steady-state point source and scattered by a spherical body is expressed in terms of an infinite sum over discrete wave numbers. In a separate paper (Hill 1972), an integral expression for this general solution is obtained by applying an exact Earth-flattening transformation to the radial part of the solution and the Watson transform to the angular part of the

solution. The far-field approximation to this integral for the scattered (reflected) field can be written as

$$\Phi \simeq \exp(i\pi/4)(2\pi\rho^*)^{-1/2} \int_{-\infty}^{\infty} \exp\{i[\kappa\rho+\eta(z+z_0)]\}\, V_s(\kappa)\frac{\kappa^{1/2}}{\eta}\, d\kappa, \qquad (3)$$

where

$\rho = a\theta$ arc distance,

$\rho^* = a(\sin\theta)$,

$\kappa = \dfrac{l+1/2}{a}$ with κ representing the horizontal (angular) component of the wave number, k, while l is a spheroidal order number,

$\eta = (k^2-\kappa^2)^{1/2}$ with η representing the vertical (radial) component of the wave number, k, and

$V_s(\kappa)$ is a spherical reflection coefficient for the radially heterogeneous medium, $r < a$.

The integral representation (1) is valid under the following conditions:

(1) $\pi > \theta > \varepsilon$ and $|\kappa a|\,\varepsilon \gg 1$; arc distance ($\rho = a\theta$) is greater than several wave lengths (the far-field approximation).

(2) $|z_0/a| \ll 1$ and $|z/a| \ll 1$; source height, z_0, and receiver height, z, above the boundary at $r = a$ are small with respect to a (see Fig. 2).

(3) $|\kappa a| \gg 1$ and $|\pi a| \gg 1$; wave lengths are much less than the radius, a, and both near-normal and near-grazing angles of incidence at $r = a$ are avoided. In the case of body waves impinging on major discontinuities in the crust and upper mantle near critical angles of incidence, these conditions are readily satisfied. Furthermore, for the outer layers of the Earth, the spherical reflection coefficient, $V_s(\kappa)$, can be approximated by a reflection coefficient computed using boundary conditions appropriate for a plane boundary at $r = a$ but with original velocity distribution in the spherical system, $c(z)$ modified according to

$$c(z) = c_s \exp(-z/a). \qquad (4)$$

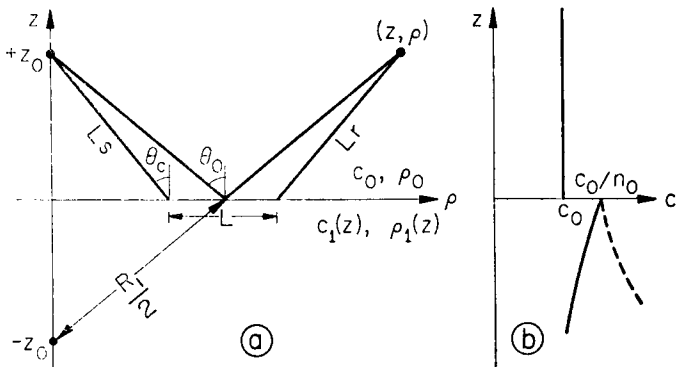

FIG. 2(a). Co-ordinate system and parameters for acoustic waves reflected from a plane boundary. The point source is at $+z_0$, the receiver at (z, ρ). (b) Acoustic velocity, c, as a function of depth. Negative- and positive-gradient cases are represented by solid and dashed lines, respectively, for $z < 0$.

This expression, which defines the exact mapping of a radial velocity distribution in a spherical geometry into a flat geometry, together with

$$z = a\,ln(r/a)$$

or

$$z \sim (r-a), \quad |z/a| \ll 1 \tag{5}$$

form the Earth-flattening transformation for the homogeneous Helmholtz equation (Hill 1972, also see Müller 1971).

Although this formulation is used to study acoustic waves in spherically symmetric radially heterogeneous fluid media, it can be applied to any heterogeneous media for which the steady-state equations of motion can be expressed as one or more uncoupled, scalar Helmholtz equations. Physically, this includes acoustic media as well as toroidal (SH) motion in elastic media, provided the radial density gradients are small with respect to the wave lengths considered; it also includes spheroidal ($P-SV$) motion, provided the displacement potential representation introduced by Richards (1971) is used, which permits approximate uncoupling of $P-SV$ motion at sufficiently high frequencies.

Approximate analytic solutions to (3) are outlined in Sections 3–5 and results obtained by exact numerical integration of (3) are summarized in Section 6. Throughout this paper the word heterogeneous will refer to continuous variations in the physical properties of a medium and the word inhomogeneous will refer to differential equations with a source term on the right.

3. The reflection coefficient $V(\kappa)$

To obtain the reflection coefficient $V(\kappa)$, we consider two fluid, inviscid half spaces joined at $z = 0$ in a Cartesian co-ordinate system $\mathbf{r} = (x, y, z)$. Let the upper half space ($z > 0$) be homogeneous with density d_0 and acoustic velocity c_0 and let the lower half space ($z < 0$) be vertically heterogeneous with density $d(z)$ and acoustic velocity $c(z)$. Because this paper is concerned with waves near the critical angles of incidence whose turning points occur at small depths below the reflecting boundary, it will be sufficient to approximate the exact curvature-mapping velocity transformation (4) in the vicinity of the boundary $r = a$ by

$$c(z) = c_0(n_0^2+\gamma z)^{-1/2}; \quad z \leqslant 0, \tag{6}$$

where the index of refraction at $z = 0$ is $n_0 = c_0/c(0_-)$ and the gradient parameter is

$$\gamma = 2n_0^2/a+\gamma_p. \tag{7}$$

The first term on the right in γ corresponds to the curvature-mapping gradient in (4), and the second term is the gradient describing the physical velocity variation for $z \leqslant 0$. The velocity gradient associated with γ for $|\gamma| \ll 1$ is

$$\beta = \frac{dc}{dz} \simeq (c_0/2n_0^3)\,\gamma. \tag{8}$$

This particular form for the velocity variation is chosen because it gives convenient solutions to the Helmholtz equation (2) in terms of Airy functions while providing a satisfactory approximation to the exact spherical mapping distribution (4) for $|z/a| \lesssim 0{\cdot}1$. Furthermore, Airy functions form the leading term in the high-frequency asymptotic solutions to (2) for more general velocity variations (Langer 1949). Thus solutions obtained using (6) will be characteristic of the high-frequency behaviour of solutions for more general velocity variations.

The density variation for $z \leqslant 0$ is taken to parallel the velocity variation or

$$d(z) = d_0(n_0^2+\gamma z)^{-1/2}. \tag{9}$$

The solutions to (2) for a plane wave incident on the boundary $z = 0$ at an angle θ in the model defined by (6) are

$$\left.\begin{aligned} &\gamma < 0 \\ &\quad \Phi(x,z) = \exp\left[i(\kappa x - \eta z)\right] + V_- \exp\left[i(\kappa x + \eta z)\right]; \quad z > 0 \\ &\quad \Phi_1(x,z) = U_- \, Ai[-\zeta(z)^{i2\pi/3}] \exp(i\kappa_1 x); \quad z < 0 \end{aligned}\right\} \tag{10a}$$

$$\left.\begin{aligned} &\gamma > 0 \\ &\quad \Phi(x,z) = \exp\left[i(\kappa x - \eta z)\right] + V_+ \exp\left[i(\kappa x + \eta z)\right]; \quad z > 0 \\ &\quad \Phi_1(x,z) = U_+ \, Ai[-\zeta(z)] \exp(i\kappa_1 x); \quad z < 0 \end{aligned}\right\} \tag{10b}$$

where

k_0 is the magnitude of the wave number in $z > 0$,

$\kappa = k_0 p$, $\eta = k_0 q$

$p = \sin\theta$, $q = \cos\theta$

$\zeta(z) = \varepsilon^{-2}(\eta_0^2 - p^2 + \gamma z)$

$\varepsilon = (\gamma/k_0)^{1/3}$

$V_\mp$ is a reflection coefficient,

$U_\pm$ is a transmission coefficient, and

$Ai(-\zeta)$ is an Airy function.

The radiation conditions imposed on these solutions as $z \to -\infty$ are such that for $\gamma < 0$ the wave field consist solely of downward propagating waves, and for $\gamma > 0$ the wave field consist of waves that decay exponentially with depth below the turning point $z = (p^2 - n_0^2)/\gamma$. These radiation conditions for the half space $z < 0$ can be related to those for the original spherical problem through the rainbow expansion (see Chapman & Phinney 1972). In particular, the above condition for $\gamma < 0$ corresponds to retaining only the first term in the rainbow expansion, or the generalized ray reflected externally at the boundary $r = a$, while the condition for $\gamma > 0$ corresponds to retaining the complete response in terms of an infinite number of generalized rays reflected internally at $r = a$.

Applying the usual boundary conditions for fluid media (continuity of pressure and the normal component of particle velocity) to (10a) and (10b) at $z = 0$ leads to the following expressions for the reflection coefficients:

$$V_- = \frac{Ai\left(-\zeta_0 \exp(i2\pi/3)\right)\left[iqm + \dfrac{\varepsilon^3}{4n_0^3 m}\right] + \exp(i2\pi/3)\,\varepsilon Ai'\left(-\zeta_0 \exp(i2\pi/3)\right)}{Ai\left(-\zeta_0 \exp(i2\pi/3)\right)\left[iqm - \dfrac{\varepsilon^3}{4n_0^3 m}\right] - \exp(i2\pi/3)\,\varepsilon Ai'\left(-\zeta_0 \exp(i2\pi/3)\right)} \tag{11a}$$

and for $\gamma > 0$

$$V_+ = \frac{Ai(-\zeta_0)\left[iqm - \dfrac{\varepsilon^3}{4n_0^3 m}\right] - \varepsilon Ai'(-\zeta_0)}{Ai(-\zeta_0)\left[iqm + \dfrac{\varepsilon^3}{4n_0^3 m}\right] + \varepsilon Ai'(-\zeta_0)}, \tag{11b}$$

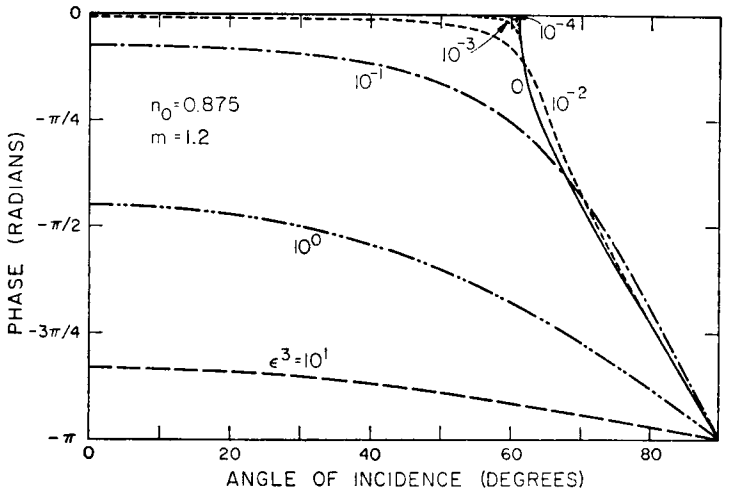

FIG. 3(a). Modulus of the plane wave reflection coefficient, V, for different values of $\varepsilon = (\gamma/k_0)^{1/3}$.

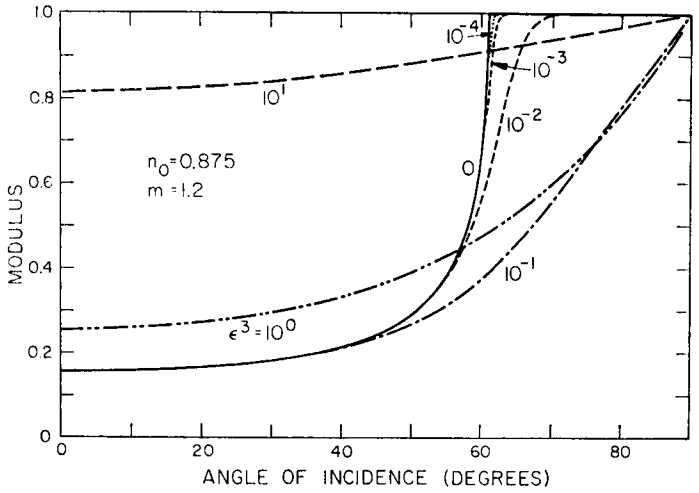

FIG. 3(b). Phase of the reflection coefficient V.

where $m = d(0)/d_0$, $\zeta_0 = \varepsilon^{-2}(n_0^2 - p^2)$, and the primes indicate derivatives of the Airy functions with respect to their arguments. These are the exact plane wave reflection coefficients for vertically heterogeneous half space defined by (6). They represent approximate reflection coefficients for the radially heterogeneous spherical medium $\gamma < a$ when the gradient parameter is given by (7). If the exact form of the spherical boundary conditions had been used instead of plane boundary conditions, a term $(2a)^{-1}$ would be included in the square brackets appearing in both the numerator and denominator of (11) (Hill 1972).

The modulus and phase of the plane-wave reflection coefficient for the negative gradient case ($\gamma < 0$) are plotted in Fig. 3 with ε as a parameter. As ε becomes very small, the modulus and phase approach the limiting values for two homogeneous

media. This can also be seen analytically by substituting the asymptotic forms of the Airy functions for $|\zeta_0| \gg 1$ into V_- and letting $\varepsilon \to 0$. The result is

$$V_0 = \frac{mq - \sqrt{(n_0^2 - p^2)}}{mq + \sqrt{(n_0^2 - p^2)}} \tag{12}$$

which is the plane-wave reflection coefficient for two homogeneous media (Brekhovskikh 1960).

The modulus of the plane-wave reflection coefficient for $\gamma > 0$ is unity. In other words, all of the energy entering the lower medium is eventually reflected into the upper, homogeneous half-space, and the reflection coefficient can be expressed as

$$V_+ = \exp\left[i2 \tan^{-1}\left(\frac{\varepsilon}{qm} \frac{A_i'(-\zeta_0)}{A_i(-\zeta_0)}\right)\right]. \tag{13}$$

For $p > n_0$ (i.e. angle of incidence greater than critical), (11b) also reduces to the homogeneous reflection coefficient when the asymptotic forms of the Airy functions are substituted. For $p < n_0$ the analogous limiting process is complicated by the diving wave phenomenon. We will consider this later.

The effect of the density gradient in the lower medium enters the reflection coefficients through the second term in the brackets multiplying $Ai(-\zeta_0 \exp(i2\pi/3))$ and $Ai(-\zeta_0)$ in (11a) and (11b), respectively. Under the assumption of small density gradients made in obtaining (5), $|mq| \gg \varepsilon^3/4{n_0}^3 m$ except when $q \sim 0$. Thus since $q = \cos\theta$, the density gradient in the lower medium has a negligible effect on the reflected wave except near grazing angles of incidence. (The same will be true for the factor $(2a)^{-1}$ introduced by using the exact spherical boundary conditions.)

4. Classification of the effects of curvature and gradients

The effects of curvature and gradients can be classified through the Earth-flattening transformation by noting that an effective null gradient ($\gamma = 0$) is associated with the critical gradient $\gamma_p = -2{n_0}^2/a$ (see equation (7)). By (8) the corresponding critical velocity gradient is $\beta_p = -c_0/a\,\mathrm{s}^{-1}$. This critical velocity gradient corresponds to the case in which the curvature of a geometrical ray at its turning point matches the curvature of the Earth (see Section 7.2.3 in Bullen (1963)). Here the ray is trapped and continues around the Earth at a constant radius. It turns out that the pure head wave occurs only in the presence of a critical velocity gradient beneath the boundary at $r = a$. This critical gradient will be used as a reference, and the cases $\gamma < 0$ and $\gamma > 0$ will be referred to as having subcritical and supercritical gradients, respectively. It follows that because of curvature, a homogeneous refractor ($\beta_p = 0$) has an effective supercritical gradient $\beta = c_0/a$. These general relations between curvature and velocity gradients are illustrated in Fig. 4.

The following terminology is adapted to describe the critically or nearly critically refracted waves for the cases illustrated in Fig. 4.

Pure head wave refers to the critical gradient case (Fig. 4(c)) or the classical, critically refracted wave at a plane boundary between homogeneous media.

Interference head wave refers to the supercritical gradient case (Fig. 4(a) and (b)) in which the 'head wave' is formed by a series of interfering *diving waves* (Cerveny & Ravindra 1971).

Diving wave refers to a generalized ray that penetrates the boundary $r = a$, is turned around in the lower medium ($r < a$) by a super-critical gradient and eventually returned to the upper medium ($r > a$).

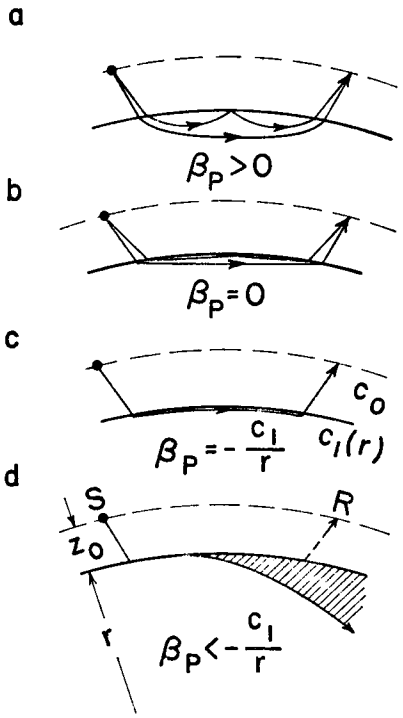

FIG. 4. Schematic representation of effects of curvature and velocity gradients on near-critical waves: (a) Positive-gradient case showing two diving waves; (b) Homogeneous case showing two diving waves; (c) Critical negative-gradient case showing classical head-wave path; (d) Subcritical gradient case showing ray shadow zone (shaded region).

Diffraction head wave refers to the subcritical gradient case (Fig. 4(d)) in which a ray shadow zone is formed between the critically refracted ray and the boundary $r = a$. Cerveny & Ravindra (1971) refer to the head wave associated with a negative velocity gradient as a 'damped head wave'. However, damping can be due to anelasticity, while diffraction accurately describes the physical process involved.

5. Analytic evaluation of the integral

We rewrite the integral (1) in the following form:

$$\Phi \simeq \exp(i\pi/4)\left[\frac{k_0}{2\pi\rho^*}\right]^{1/2} \int_{-\infty}^{\infty} \exp\{ik_0[\rho p + q(z+z_0)]\}\, V \frac{p^{1/2}}{q}\, dp. \qquad (14)$$

Here the spherical reflection coefficient $V_s(\kappa)$ is replaced by V, which represents V_-, V_+, or V_0, and the variable of integration is changed to p according to $\kappa = k_0 p$. The integrand has branch points at $p = \pm 1$ associated with the radical $q = \sqrt{(1-p^2)}$ and at $p = 0$ associated with $\sqrt{p}$. We choose the branch cuts such that

$$-\pi/2 < \arg(q) \leqslant \pi/2$$

$$-\pi/2 < \arg(\sqrt{p}) \leqslant \pi/2$$

on the upper Reimann sheet. The location of these branch cuts in the complex p-plane together with the original integration path are illustrated in Fig. 5.

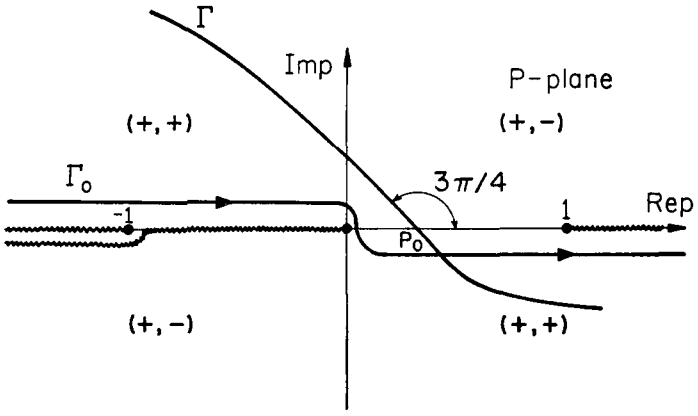

FIG. 5. Branch cuts and original contour for Weyl integral in the complex p-plane. $(+,-)$ indicates signs of real and imaginary parts of the radical $\sqrt{(1-p^2)}$ in each quadrant.

When V is a slowly varying function of p, (14) can be evaluated by the saddle point method. In this case the steepest descents path, Γ, passes through the saddle point at $p = p_0 = \sin\theta_0$ as shown in Fig. 5, and standard methods lead to

$$\Phi_r \simeq \frac{\exp(ik_0 R_1)}{R_1} V(p_0), \tag{15}$$

This expression gives the geometrical ray theory approximation to waves reflected from the boundary $z = 0$ at an angle of incidence θ_0. (See Section 19 in Brekhovskikh 1960).

5.1 *Subcritical gradient*

The reflection coefficient V_- (11a) has a line of poles that extends from near $p = n_0$ into the first quadrant of the complex p-plane at an angle of $\pi/3$, as shown in Fig. 6 (see Appendix I). It is clear from Fig. 6 that when $p_0 < n_0$, the only contribution to (14) comes from the saddle point p_0. When $p_0 > n_0$, however, the

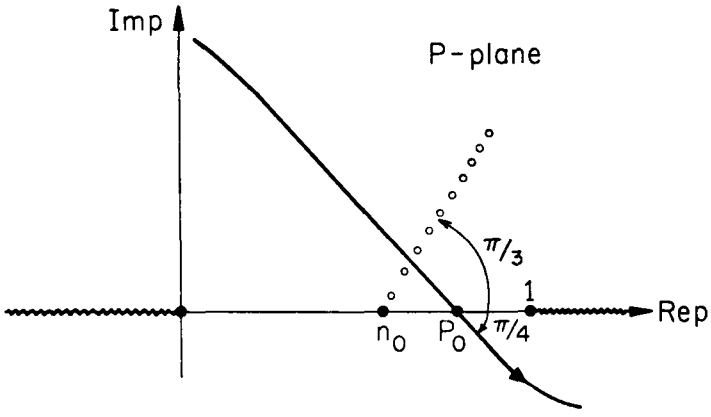

FIG. 6. Steepest-descents path and head-wave poles in complex p-plane for negative gradient case. P_0 is saddle point, n_0 index of refraction at boundary.

steepest-descents path through p_0 passes through the line of poles associated with V_-. In this case, there will be contributions to (14) from both the saddle point, p_0, which describes the reflected wave field (15), and the poles of V_-, which describe the diffraction head wave. These 'separate' contributions to the total wave field are indicated as follows

$$\Phi_- = \begin{cases} \Phi_{r-}; & p_0 < n_0 \\ \Phi_{r-} + \Phi_{h-}; & p_0 > n_0 \end{cases} \tag{16}$$

where Φ_{r-} is given by (15) with $V(p_0)$ replaced by $V_-(p_0)$, and Φ_{h-} is the contribution from the poles giving the diffraction head wave. For nearcritical angles of incidence ($p_0 > n_0$) the phase difference between these 'separate' contributions is small, and it is not meaningful to make a distinction between Φ_{r-} and Φ_{h-}. The contributions of the poles of V_- to (14) decrease exponentially with their distance from the real p axis such that the dominant contribution comes from poles in the vicinity of $p = n_0$. Furthermore, the contributions with phase velocities near the head-wave phase velocity are limited to the poles in the vicinity of $p = n_0$. Applying the residue theorem to those poles in the region $|p-n_0| \ll 1$, we obtain

$$\Phi_{h-}(r, z, \omega) \simeq \sqrt{\left(\frac{2\pi k_0}{n_0 \rho}\right)} \frac{\varepsilon^3 \exp\left[i(\phi_0 + \pi/4)\right]}{m(1-n_0^2)} \sum_{j=1}^{N} \exp\left[i \frac{k_0 L \varepsilon^2 a_j \exp(i\pi/3)}{2n_0}\right], \tag{17}$$

where a_j is the j-th zero of $Ai(-\tau)$, ϕ_0 is the pure head wave phase given by

$$\phi_0 = k_0(L_r + L_s) + k_1 L$$

and the ray path distances L_r, L_s, and L are as illustrated in Fig. 2 (see Appendix I).

This expression can be recast into more meaningful forms for two limiting cases. We define

$$\sigma_- = i\left(\frac{3\pi}{8}\right)^{2/3} \frac{k_0 L \varepsilon^2}{2n_0} \exp(i\pi/3) \tag{18}$$

and consider the cases for which $|\sigma_-| \ll 1$ and $|\sigma_-| \gg 1$.

For $|\sigma_-| \ll 1$ the series (17) can be summed using the Euler–MacLaurin summation formula and the integral representation of the incomplete gamma function (Abramowitz & Stegun 1964, p. 262). In the limit as $\varepsilon^2 \to 0$, the result is

$$\Phi_{h-} \simeq \left[\frac{2in_0 \exp(i\phi_0)}{k_0 m(1-n_0^2) p^{1/2} L^{3/2}}\right] \left\{1 - \sigma_-^{3/2} \exp(-\alpha_-) \sum_{n=0}^{\infty} \frac{\sigma_-^n}{\Gamma(n/2+n)} - (g_-)^{-1}(\tfrac{1}{2} + \tfrac{1}{6}\sigma_- + \ldots)\right\} \tag{19}$$

where

$$g_- = \sqrt{\left(\frac{2}{\pi k_0}\right)\left(\frac{n_0 \sigma_-}{L}\right)^{3/2}} \gamma^{-1} \exp(i\pi/4)$$

(Hill 1971b). The term in the square brackets is the pure head-wave potential for the case in which the lower medium is homogeneous (see Brekhovskikh 1960). This result is valid in the limit of small ε, but at large distances from the critical point, many terms in the series must be included. At relatively small distance from the critical point, such that $|\sigma_-| \ll 1$, the diffraction head wave is given by the product of the pure head wave and the correction term $(1-\sigma_-^{3/2})$. In the immediate vicinity of the critical point itself, (19) is invalid because of the interaction of the saddle point and head wave poles. However, $|\sigma_-|$ become negligibly small as the critical point

is approached, and the theory for waves reflected and refracted from a homogeneous medium in the immediate vicinity of the critical point by Cerveny (1965) will provide a good approximation in the case of small velocity gradients as well.

When $|\sigma_-| \gg 1$, the dominant contribution to (14) comes from the pole nearest the real p-axis, and the diffraction head wave is given by the first term in (17), or

$$\Phi_{h-} \simeq -\frac{2\pi k_0}{\rho} \frac{\varepsilon^3 \exp\left[i(\phi_0+\chi_I+\pi/4)\right]}{m(1-n_0^2)} \times \exp\left[-\frac{\sqrt{3}}{4}\frac{k_0 L\varepsilon^2}{n_0}\left(a_1+\frac{\varepsilon}{\sqrt{(3)}m\sqrt{(1-q^2)}}\right)\right].$$

Thus at large distances from the critical point ($L \gg 1$), the diffraction head wave spectral amplitude decays exponentially as ($\varepsilon^2 L$), and is slightly dispersed by the negative velocity gradient. In particular, at large distance, the horizontal phase velocity of the diffraction head wave is approximately given by

$$c_{h-} \simeq c_0/\sin\left(n_0+\frac{k_0 L\varepsilon^2 a_j}{4n_0}\right).$$

5.2 *Supercritical gradient*

The reflection coefficient V_+ (11b) has a line of poles that lies just above the real p axis in the interval $0 < p < n_0$, as shown in Fig. 7 (see Appendix II). As before, there will be two 'separate' contributions to (14) when $p_0 > n_0$: one from the saddle point p_0, which gives the field reflected by the boundary (15), and the other from the line of poles crossed by the steepest descents path, which gives the interference head wave. The saddle point method cannot be directly applied when $p_0 < n_0$, however, because the standard form of the saddle point is distorted by the adjacent poles. This difficulty can be avoided by representing V_+ as an infinite series over the interval $0 < p < n_0$ and evaluating each term by the saddle point method.

These 'separate' contributions to (14) in the case of a supercritical velocity gradient are indicated as follows

$$\Phi_+ = \begin{cases} \Phi_{r+}+\Phi_d; & p_0 < n_0 \\ \Phi_{r+}+\Phi_{h+}; & p_0 > n_0 \end{cases} \tag{21}$$

where ϕ_r is given by (15) with $V_+(p_0)$ in place of $V(p_0)$, Φ_d is the sum of saddle point contribution from the series expansion of V_+, and Φ_{h+} is the contribution from the poles of V_+ giving the interference head wave.

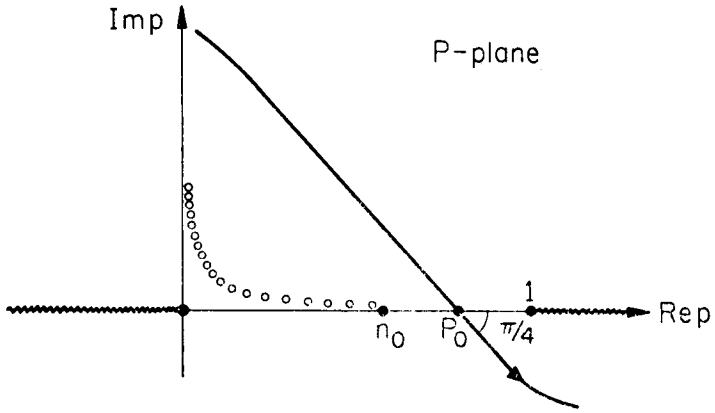

FIG. 7. Steepest-descents path and diving wave poles in complex p-plane for positive gradient case.

All the poles in the interval $0 < p < n_0$ contribute to Φ_{n+} when $p_0 > n_0$ (see Fig. 7). These poles describe normal modes leaking into the overlying homogeneous half-space and propagating in the wave guide formed between the discontinuity in velocity of $z = 0$ and the continuous increase in velocity at depth. The poles in the vicinity of $p = n_0$ are associated with normal modes that have phase velocities near the pure head wave phase velocity. The poles closer to the origin describe deeply penetrating normal modes with high phase velocities and low group velocities. To obtain an approximate expression for the interference head wave, we consider only the contribution from poles in the region $|p-n_0| \ll 1$ to obtain

$$\Phi_{h+} \simeq -\exp(i/4)\sqrt{\left(\frac{2\pi k_0}{\rho n_0}\right)}\,\varepsilon^3 \exp\left[i\phi_0 - \frac{k_0 L\varepsilon^3}{2n_0 qm}\right] \sum_{j=1}^{N} \exp\left\{-i\frac{k_0\varepsilon^2}{2n_0}a_j\left[L - \frac{iL^*\varepsilon^3}{{n_0}^2 q_c m} + \frac{L^*\varepsilon^2 a_j}{2n_0}\right]\right\} \quad (22)$$

where $L^* = (L+\rho_c/{q_c}^3)$, $q_c = \cos\theta_c$, ρ_c is the critical distance, N is the number of poles in $|p-n_0| \ll 1$ and the remaining parameters are as in (17) (see Appendix II).

To identify the head wave-like contribution from the poles, we proceed as before by introducing a parameter

$$\sigma_+ = \frac{k_0 L\varepsilon^2}{2n_0} \quad (23)$$

and applying the Euler–MacLaurin summation formula. The summation process, which in this case involves identifying the Euler–MacLaurin integral as the integral representation for a parabolic cylinder function of three-halves order, can be shown to result in an expression of the following form for $|\sigma_+| \ll 1$ (Hill 1971b)

$$\Phi_{n+} \simeq \left[\frac{2in_0 \exp(i\phi_0)}{k_0 m(1-{n_0}^2)\rho^{1/2} L^{3/2}}\right] \cdot [1+\varepsilon\sigma_+ g + O(\varepsilon{\sigma_+}^2)], \quad (24)$$

where

$$g = \exp(-i\pi/4)\sqrt{\left(\frac{\pi k_0 L}{2n_0}\right)}\left\{1/2+\exp\left[i\left(\frac{3\pi}{8}\right)^{2/3}\sigma_+\right]\right\} - \frac{1}{q_c m}.$$

This expression is analogous to (19) for the subcritical gradient case. It shows that at small distances, L, beyond the critical point, the interference head wave is like the pure head wave plus a correction term. As L increases for a given frequency, however, it becomes necessary to include additional terms of increasing order in σ_+ in (24). This rapidly becomes impractical because of the complicated nature of the higher-order terms, and at large distances becomes convenient to describe the wave field in terms of the series Φ_d.

To obtain the representation Φ_d, the reflection coefficient $V_+(p)$ (11b) is expanded into an infinite series, the n-th term of which can be identified as the reflection coefficient for the generalized ray bottoming n times in the heterogeneous medium and reflecting $(n-1)$ times at the boundary $z = 0$. The expansion is accomplished by replacing the standing wave form of the Airy function appearing in (11b) with a combination of Airy functions representing upgoing and downgoing travelling waves

(equation 10.4.7 in Abramowitz & Steugn 1964) and forming the following Airy function ratios

$$\left.\begin{aligned} \mathscr{A}^{(1)} &= Ai'(-\zeta_0 \exp(i2\pi/3))/Ai(-\zeta_0 \exp(i2\pi/3)) \\ \mathscr{A}^{(2)} &= Ai'(-\zeta_0 \exp(-i2\pi/3))/Ai(-\zeta_0 \exp(-i2\pi/3)) \\ \mathscr{A} &= Ai(-\zeta_0 \exp(i2\pi/3))/Ai(-\zeta_0 \exp(-i2\pi/3)). \end{aligned}\right\} \tag{25}$$

For real angles of incidence ($|p| < 1$) $V_+(p)$ can then be written as

$$V_+(p) = Y_0 + \sum_{n=1}^{\infty} Y_n, \tag{26}$$

where

$$Y_0 = \frac{\left(iqm - \dfrac{\varepsilon^3}{4{n_0}^2 m}\right) - \varepsilon \exp(-i2\pi/3)\,\mathscr{A}^{(2)}}{\left(iqm + \dfrac{\varepsilon^3}{4{n_0}^2 m}\right) + \varepsilon \exp(-i2\pi/3)\,\mathscr{A}^{(2)}}$$

$$Y_n = (-1)^{n-1}\, 2iqm \exp(in/3)\,\mathscr{A}^n[\mathscr{A}^{(1)} \exp(-i2\pi/3)\,\mathscr{A}^{(2)} \exp(-i2\pi/3)] \times \frac{\left[\left(iqm + \dfrac{\varepsilon^3}{4{n_0}^2 m}\right) + \varepsilon \exp(i2\pi/3)\,\mathscr{A}^{(1)}\right]^{n-1}}{\left[\left(iqm + \dfrac{\varepsilon^3}{4{n_0}^2 m}\right) + \varepsilon \exp(-i2\pi/3)\,\mathscr{A}^{(2)}\right]^{n+1}}.$$

When substituted into the integral (14), this series representation of the reflection coefficient provides a complete description of the reflected field in terms of an infinite number of generalized rays. The singularities associated with each term in the series involve a line of poles extending from $p = n_0$ into the lower half of the complex p-plane at an angle of $-\pi/3$. The singularities are simple poles for Y_0 and poles of order $(n+1)$ for the n-th term under the summation sign in (26).

An approximate expression for the reflected field at large distances can be obtained by replacing the Airy function ratios in (26) by their asymptotic forms for $|\zeta_0| \gg 1$ (10.4.59–10.4.68 in Abramowitz & Stegun 1964), putting (26) into (14), and interchanging the order of integration. Thus

$$\Phi_{r+} \sim \exp(i\pi/4) \sqrt{\left(\frac{k_0}{2\pi\rho^*}\right)} \int_{-\infty}^{\infty} \exp[(ik_0)(p+q(z+z_0))]\, V_0 \frac{\sqrt{p}}{q}\, dp \tag{27}$$

and

$$\Phi_d \sim -\exp(i\pi/4) \sqrt{\left(\frac{k_0}{2\pi\rho^*}\right)} \sum_{n=1}^{\infty} \exp(in\pi/2) \int_{-\infty}^{\infty} \exp[ik_0 f_n(p)]\, {V_0}^{n-1}(1-{V_0}^2) \frac{\sqrt{p}}{q} \tag{28}$$

with

$$f_n(p) = \left[\rho p + q(z+z_0) + \frac{4n}{3\gamma}({n_0}^2 - p^2)^{3/2}\right].$$

Here V_0 is the plane wave reflection coefficient (12). As suggested in (21), the first integral (27) describes waves reflected by the boundary $z = 0$, and its saddle point evaluation is given by (15). The series (28) describes the infinite number of diving waves reflected by the positive velocity gradient in $z < 0$.

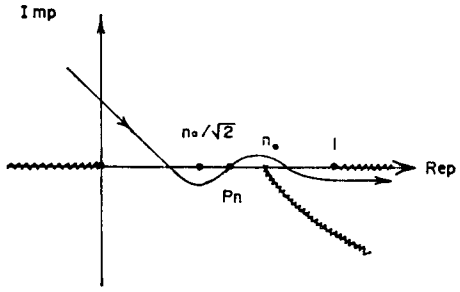

FIG. 8. Branch cuts and steepest descents path for n-th diving wave generalized ray expansion of reflection coefficient for positive gradient.

Each integral in (28) has a pair of branch points at $p = \pm n_0$ associated with the radical $(n_0^2 - = p^2)^{3/2}$ in $f_n(p)$ in addition to the branch points at $p = \pm 1$ and $p = 0$ described earlier. These new branch cuts are the asymptotic equivalents of the lines of poles associated with the exact series representation of V_+ (26). To insure that the integrals in (28) will be convergent along the original integration path $-\infty < p < \infty$, these new branch cuts are chosen to follow the lines defined by the poles (see Fig. 8) by requiring $-4\pi/3 < \arg [n_0^2 - p^2)^{3/2}] < 2\pi/3$.

The saddle point for the n-th term in (28) is given by

$$\frac{d}{dp} f_n(p) = 0$$

or

$$\left[\rho - \frac{p}{(1-P^2)^{1/2}}(z+z_0) - \frac{4n}{\gamma} p(n_0^2 - p^2)^{1/2}\right] = 0. \tag{29}$$

As can be seen from the geometrical ray relations illustrated in Fig. 9 (29) is satisfied by $p = p_n = \sin\theta_n$. Thus the saddle point, p_n, for the n-th term in (28) is the sine of the angle of incidence, θ_n, for the diving wave entering the lower medium and bottoming n times beneath the boundary $z = 0$ before arriving at the point $\mathbf{r} = (\rho, z)$. The

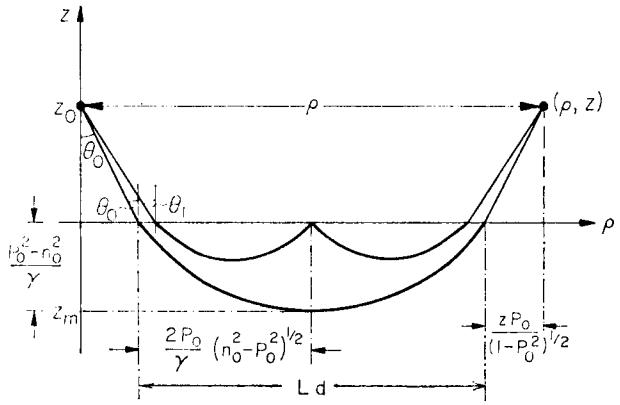

FIG. 9. Parameters and geometry of direct (P) and once-reflected diving (PaP) rays in the case of a positive gradient in the lower medium. The source and receiver at $(0, z_0)$ and (ρ, z), respectively.

steepest descents path for this integrand approaches the saddle point at an angle of $-3\pi/4$ for $n_0/\sqrt{(2)} < p_n < n_0$ and $3\pi/4$ for $p_n < n_0/\sqrt{2}$, as illustrated in Fig. 8. As no singularities are crossed in deforming the contour, the entire contribution for each term in the series comes from the immediate vicinity of the respective saddle points.

Evaluating (28) by the saddle point method we obtain

$$\Phi_d^{(n)} \simeq \exp\left[ik_0 f_n(p_n) + i\pi(n-1)/2\right]$$

$$\times \left[\left(\frac{\gamma}{\rho^*}\right) \frac{p_n(1-p_n)^{3/2}(n_0^2-p_n^2)^{1/2}}{4(n)q_n^3(n_0^2-2p_n^2)-\gamma(n_0^2-p_n^2)^{1/2}(z+z_0)}\right]^{1/2} \frac{V_0^{(n-1)}(1-V_0^2)}{q_n} \tag{30}$$

$$q_n = (1-p_n^2)^{1/2},$$

for $n_0/\sqrt{(2)} < p_n < n_0$. Here $f_n(p_n)$ is given in (28) and $V_0(p_n)$ is given by (12). This result expresses the geometrical ray-theory phase and amplitude for diving waves that bottom n times in the heterogeneous medium at depths less than $z = -n_0/(2\gamma)$. The result for $p_n < n_0/\sqrt{2}$, which describes diving waves that bottom at depths greater than $z = -n_0/(2\gamma)$, is the same as (30) but with the phase factor $\exp[i\pi(n-1)/2]$ replaced by $\exp(-i\pi n/2)$. These deeper diving waves form a caustic that intersects the surface ($z \simeq z_0$) where the direct diving wave ($n = 1$) with an angle of incidence corresponding to $p_1 = n_0/\sqrt{2}$ emerges; the difference in the phase factor describes the $-\pi/2$ phase shift acquired by these waves as they pass through the caustic (Tolstoy 1968).

This caustic for waves with angles of incidence corresponding to $p_n \lesssim n_0/\sqrt{2}$ is a result of the particular velocity distribution chosen in this paper (equation (6)). In general, a similar caustic will occur in any half space in which the velocity gradient increases monotonically with depth (e.g. equation (6) or the exact Earth-curvature mapping distribution, equation (4)), whereas such a caustic will not occur in a medium with a constant positive gradient or a positive gradient that decreases monotonically with depth. The primary concern in this paper is with the effect of small gradients on waves near the critical angle of incidence; we will thus limit our consideration of diving waves (30) with $n_0/\sqrt{(2)} < p_n < n_0$. These waves are not involved with the caustic formed by the more deeply penetrating diving waves, and they provide a reliable analogue of the family of chord waves in the Earth reflected internally at the boundary $r = a$ for moderate epicentral distances ($\Delta \lesssim 20$–30 degrees).

Note that the phase of the n-th diving wave differs from the geometrical ray theory phase $k_0 f_n(p_n)$, by $\pi(n-1)/2$. Physically, this can be attributed to a $\pi(n-1)$ phase shift acquired by $(n-1)$ internal reflections at the boundary $r = a$ and $a-\pi(n-1)/2$ phase shift associated with $(n-1)$ internal caustics formed by the multiply reflected waves. Thus the phases of P, PaP, $P2aP$ are 0, $\pi/2$, and π with respect to the geometrical ray theory phase.

The range of validity of the diving wave result is limited by two approximations. The first is the assumption that $|\zeta_0| \gg 1$ made in obtaining the asymptotic form of the reflection coefficient. For most purposes, it will be adequate to take

$$|\zeta_0| = \left|\left(\frac{k_0}{\gamma}\right)^{2/3}(n_0^2-p_n^2)\right| > 3.$$

Using the geometrical ray theory results illustrated in Fig. 7, this restriction can be translated into limitations on the minimum depth of penetration by the diving wave below the boundary, $z = 0$, or

$$z_{\min} \sim 3(\gamma k_0^2)^{-1/3} \tag{31}$$

and the minimum horizontal distance travelled by the diving wave in the lower medium, or

$$\rho_{\min} \sim 2\frac{p_n(z+z_0)}{(1-p_n^2)^{1/2}} + \frac{4\sqrt{(3)n}}{(k_0\gamma^2)^{1/3}}(\gamma z_{\min}+n_0^2). \tag{32}$$

The second approximation comes from retaining only the first term in the steepest descents evaluation of the integral; this is the geometrical ray-theory approximation. To obtain a frequency dependent correction to the geometrical ray-theory approximation, it is necessary to include the next term in the steepest-descent result, which is of order (γ/k_0).

The results for the effect of a supercritical gradient on refracted waves can be summarized as follows:

(1) At relatively short distances beyond the critical distance, such that $L \ll 2n_0/(k_0\gamma^2)^{1/3}$, the interference head wave can be represented by (22) as a sum of normal modes propagating between the discontinuous boundary and the underlying positive gradient and leaking into the overlying half space. The combination of these modes results in a wave with the properties of a pure head wave plus a correction of order σ_+.

(2) At sufficiently large distances beyond the critical distance, such that $L_d > (4/3)p_0/(k_0\gamma^2)^{1/3}$, the refracted field can be described as a sum of diving waves

$$\Phi_d = \sum_{n=1}^{\infty} \Phi_d^{(n)}$$

where $\Phi_d^{(n)}$ is given by (30) in the ray-theoretical limit ($|\gamma/k_0| \ll 1$); and L_d is the horizontal distance covered by the direct diving wave. By (31), the expression for any given diving wave, $\Phi_d^{(n)}$, will be valid as long as the wave bottoms at a depth greater than at least $z_m \simeq (\lambda^2/\gamma)^{1/3}$ beneath the boundary $z = 0$ and does not touch the caustic defined by $p_n = n_0/\sqrt{2}$.

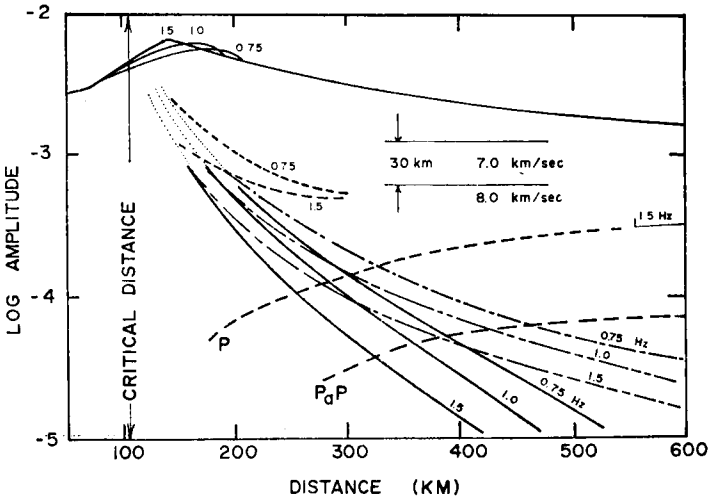

FIG. 10. Theoretical amplitudes for reflected and refracted waves from a plane boundary and vertically heterogeneous half-space. Both source and receiver are 30 km above the boundary at which $n_0 = 0{\cdot}875$, $m = 1{\cdot}2$. Dash–dot curves are pure head-wave amplitudes ($\gamma = 0$); heavy solid curves are diffraction head-wave amplitudes for negative gradient ($\gamma = -10^{-3}\,\mathrm{km}^{-1}$); short dashed curves are envelopes of amplitude curves for the interference head wave ($\gamma = 10^{-3}\,\mathrm{km}^{-1}$); long dashed curves are amplitudes of direct (P) and once reflected (PaP) diving waves.

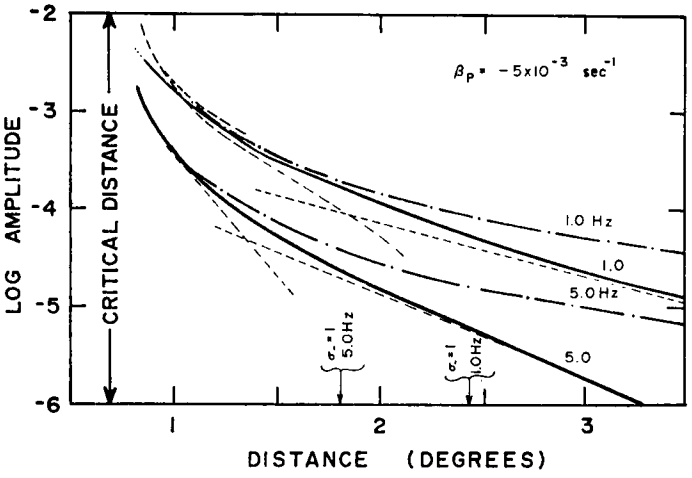

FIG. 11(a). Comparison of exact numerical solutions (solid lines) and asymptotic solutions (dashed lines) for head waves from a spherical boundary with a subcritical velocity gradient in the lower medium. Short and long-dashed lines indicate asymptotic solution for $|\sigma_-| \ll 1$ and $|\sigma_-| \gg 1$, respectively. Exact solution for pure head waves are indicated by dash–dotted curves for reference. Both source and receiver are 30 km above the boundary at which $n = 0{\cdot}80$, $m = 1{\cdot}2$.

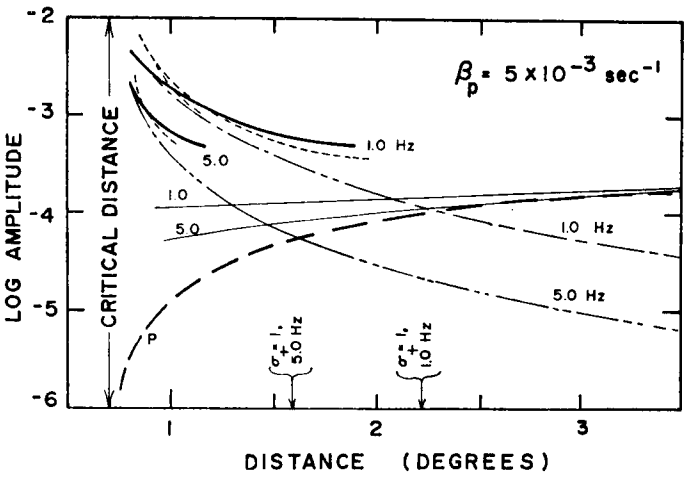

FIG. 11(b). Comparison of exact numerical solutions and asymptotic solutions for diving waves from the same model as in 11(a), but with a positive velocity gradient in the lower medium. Heavy lines are envelopes for exact diving wave amplitudes; short-dashed lines are asymptotic solutions for $|\sigma_+| \ll 1$; long-dashed line is ray-theoretical amplitude for direct diving wave; light solid lines are exact amplitudes for direct diving wave.

At sufficiently large distances, the direct diving wave will arrive first and will be followed at successively later times by waves making an increasing number of internal reflections at the boundary $r = a$. The direct diving wave (P) will have the same wave form as the source, and the diving wave internally reflected once at the boundary $r = a$ (PaP) will have a wave form modified by a $\pi/2$ phase shift in agreement with results for the analogous phases P and PP in a homogeneous sphere (Jeffreys & Lapwood 1957).

The last group of diving waves to arrive will be those that propagate just below the boundary making a great number of internal reflections. Their travel time will be essentially that of a pure head wave. These boundary-layer waves, which can be regarded as the interference head wave at large distances, are described by the first term in the normal mode equation (22). The amplitude of this interference head wave is small with respect to the first few diving waves, and in practice, would be difficult to identify.

5.3 *The critical gradient*

In the special case of a critical gradient [$\gamma_p = -(2n_0^2/a)$] the reflection coefficient reduces to the form for a homogeneous half-space (12). Methods for the asymptotic evaluation of the integral (14) with $V(p)$ given by (12) are well known and are described in Brekhovskikh (1960) or Grant & West (1965). The saddle point contribution describing the reflected wave is given by (15), and the pure head-wave, which arises from the branch cut associated with the radical $(n_0^2 - p^2)^{1/2}$ in (12), is given by the term in the square brackets in (19).

6. Numerical results

In this section we will compare numerical results based on both the analytic asymptotic expressions obtained for the refracted and reflected waves as well as results obtained by exact numerical integration of the integral (14) containing the appropriate reflection coefficients for some specific models. The consideration of both asymptotic solutions and exact numerical solutions together often provides insight into a problem that would not necessarily be realized through either approach by itself. The method of numerical integration used is similar to that described by Phinney & Cathles (1969), Richards (1970), or Chapman & Phinney (1972). The Airy functions occurring in the reflection coefficients were numerically evaluated using SHARE subrouting HF13 (Berry 1964).

Fig. 10 summarizes the basic results obtained by numerical integration of (14) in terms of amplitudes of reflected and refracted waves from a plane boundary as a function of distance from the source. In this model both source and receiver are at a height of 30 km above the boundary, across which the acoustic velocity increases from 7·0 to 8·0 km s^{-1}. Theoretical amplitudes were computed for three frequencies (0·5, 1·0, and 5 Hz) and three values of the gradient parameter in the lower half-space ($\gamma_p = 0$, and $\pm 10^{-3}$ km^{-1}). Because in this case the boundary is flat, $a \to \infty$, $\gamma \to \gamma_p$, $\rho^* \to \rho$ and (14) reduces to the far-field form of the Weyl integral.

Amplitude curves for the homogeneous case ($\gamma_p = 0$) illustrate the properties of reflected waves and pure head waves described earlier by Cerveny (1965, 1966). Note in particular the frequency-dependent shift of the maximum in the reflected wave amplitude away from the geometrical ray critical point, which is located at 108 km in this model. The reflected wave amplitudes are insensitive to small velocity gradients in the lower half-space, and the amplitude curves for the reflected waves plotted in Fig. 10 apply for $\gamma_p = \pm 10^{-3}$ km^{-1} as well as for $\gamma = 0$.

The amplitudes obtained by numerical integration of (14) for the diffraction head wave and interference head wave ($\gamma_p = -10^{-3}$ and $+10^{-3}$, respectively) confirm

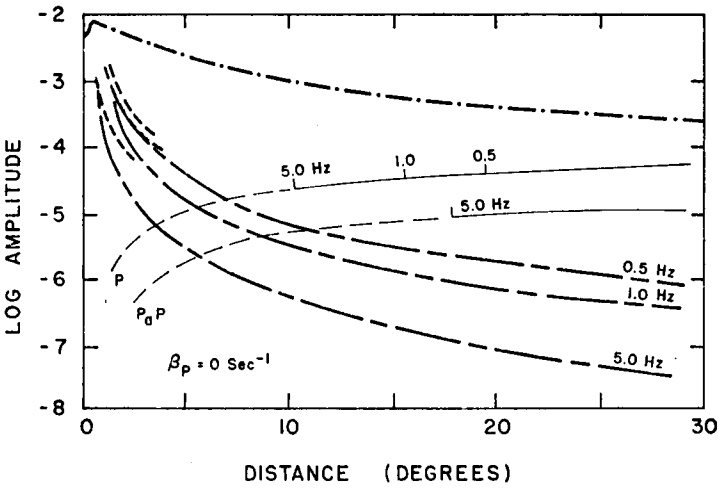

FIG. 12. Theoretical amplitude curves for reflected and refracted waves from a spherical *M*-discontinuity and a homogeneous, 8·0 km s^{-1} mantle; source and receiver are 30 km above the *M*-discontinuity in a 6·4 km s^{-1} 'crust'. Solid lines are ray-theoretical amplitudes for direct (*P*) and once-reflected (*PP*) diving waves; vertical bars show minimum distance for valid description for wave of indicated frequency. Heavy dashed lines indicate envelopes of interfering diving-wave amplitudes. Heavy long-dashed–short-dashed lines show pure head-wave amplitudes and heavy dash–dotted line is the reflected-wave amplitude.

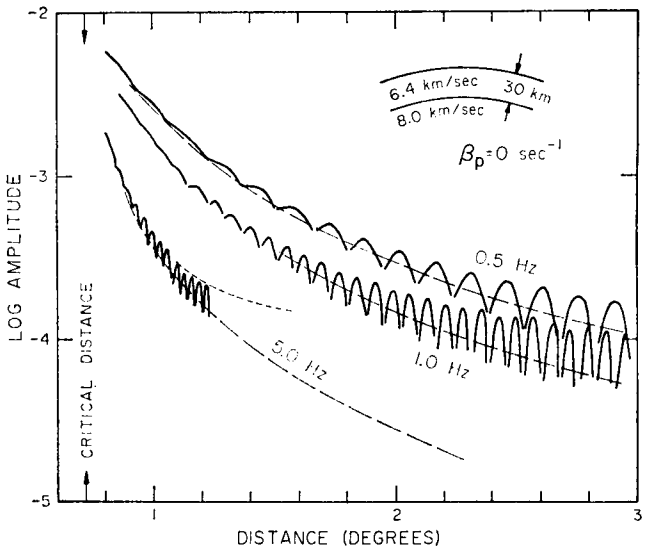

FIG. 13. Details of exact numerical solution for interference head wave amplitudes in model described in Fig. 12. Dashed lines are pure head-wave amplitudes.

the general behaviour predicted by the asymptotic solutions (19), (20), and (24). The exact numerical results, however, reveal that the amplitude curves for the interference head wave have a scalloped character not predicted by the first two terms in the asymptotic result (24). The curves plotted in Fig. 10 for the interference head wave are the upper envelopes of the scalloped curves; examples illustrating the details of the scalloping are presented below.

The ray-theoretical amplitudes of the first two diving waves for the positive gradient computed using (30) are also plotted in Fig. 10. According to the criteria given by equations (31) and (32), the ray theory amplitudes for the direct diving wave (*P* in Fig. 10) becomes valid beyond 550 km at 1·5 Hz and the amplitudes of the lower frequency components of the direct diving wave as well as the once-reflected diving wave (*PaP* in Fig. 10) become valid at distances beyond 600 km.

The remaining computations are based on a spherical Earth model composed of a 'crust' 30 km thick with acoustic velocity of 6·4 km s^{-1} and a mantle with a velocity of 8·0 km s^{-1} just below the *M* discontinuity at a radius of 6367 km. The source and receiver are located on the 'surface' 30 km above the *M* discontinuity, although, as indicated earlier, the effects of a free surface are not included in the computations.

A comparison of approximate analytical solutions with exact results obtained by numerical integration of (14) is presented in Fig. 11(a) and (b) for subcritical ($\beta_p = -5\times10^{-3}$) and supercritical ($\beta_p = 5\times10^{-3}$) gradients, respectively. Exact amplitude curves for the pure head wave are plotted in both figures for reference.

In both cases asymptotic solutions for $|\sigma_-| \ll 1$ or $|\sigma_+| \ll 1$ provide only fair approximations to the exact results if all but the lowest order terms in σ_- and σ_+ are neglected in (19) and (24). In contrast, the asymptotic solutions for the diffraction head wave (20) and the direct diving wave (30 with $n = 1$) provide fair approximations to the exact results when $|\sigma_-|$ and $|\sigma_+| \sim 1$, and arbitrarily good approximations for increasing values of $|\sigma_-|$ and $|\sigma_+|$. By (33), the asymptotic solution for the direct diving wave (*P*) should only be valid beyond about 3 degrees for a 5 Hz wave. The

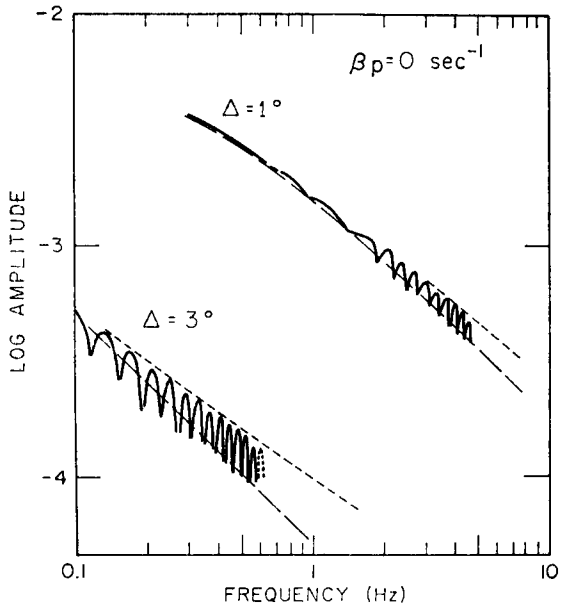

FIG. 14. Spectral amplitudes of interference head wave at distances of 1·0 and 3·0 degrees for model described in Fig. 13. Dashed lines are pure head-wave spectra.

results plotted in Fig. 11(b), however, show good agreement with the exact beginning about 2·5 degrees. Evidently (32) and (33) are rather conservative criteria for the validity of (30).

Theoretical amplitude curves for 0·5, 1·0, and 5·0 Hz waves in an Earth model with a homogeneous mantle ($\beta = 1{\cdot}25 \times 10^{-3}$, $\beta_p = 0$) and models with mantle velocity gradients of $\beta_p = \pm 5 \times 10^{-3}$ and $\beta_p = \pm 1 \times 10^{-2}\,s^{-1}$ are plotted in Figs 12, 15, and 16, respectively. These figures serve to illustrate the sensitivity of the diffraction head wave, interference head wave, and diving wave amplitudes to different velocity gradients.

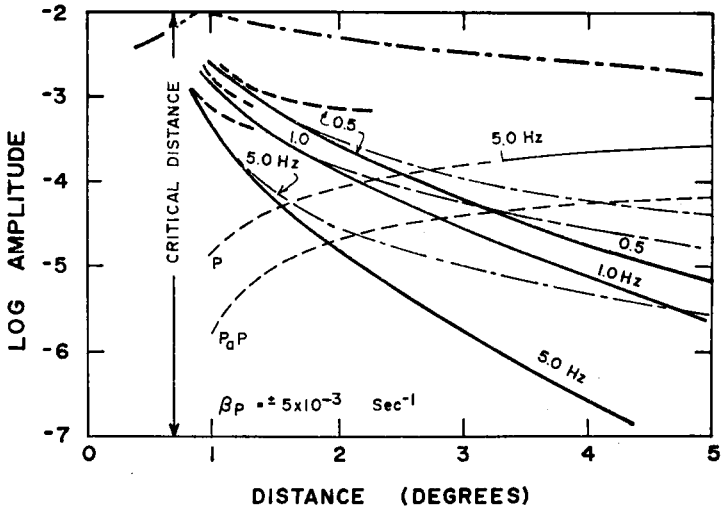

FIG. 15. Theoretical amplitude curves for reflected and refracted waves in same model as in Fig. 12 but with negative and positive velocity gradients in mantle of $\pm 0{\cdot}5 \times 10^{-3}\,s^{-1}$. Heavy solid lines are head-wave amplitudes in negative gradient case; code for curves in positive-gradient case is the same as in Fig. 15.

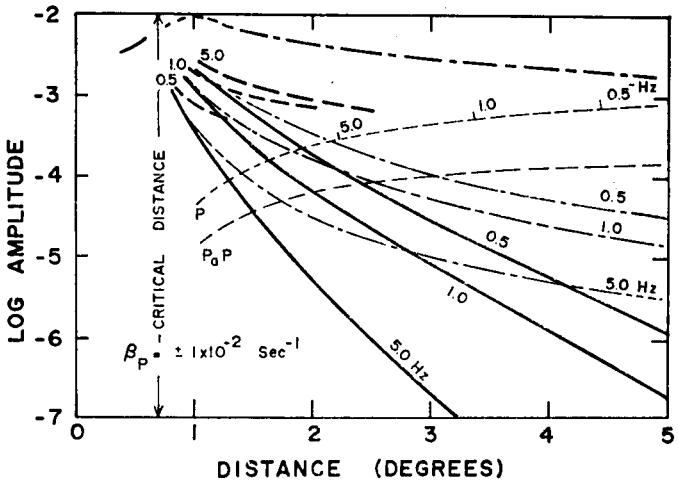

FIG. 16. Theoretical amplitude curves for reflected and refracted waves in same model as in Figs 12 and 15 but with positive and negative velocity gradients in the mantle of $\pm 1 \times 10^{-3}\,s^{-1}$. Code for curves is same as in Figs 12 and 15.

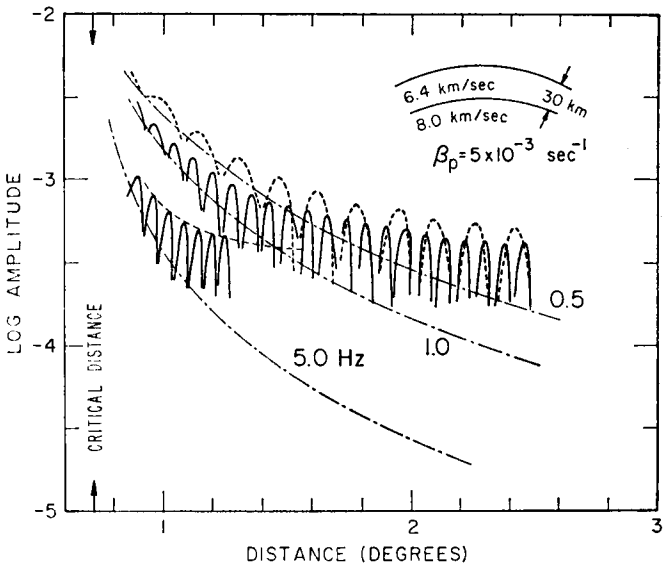

FIG. 17. Details of exact numerical solution for interference head wave amplitudes for model in Fig. 15 with a positive gradient 5×10^{-3} s^{-1}.

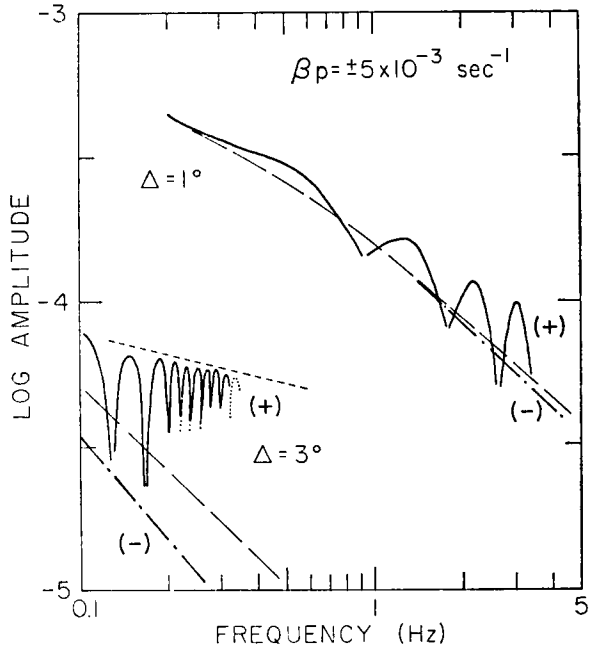

FIG. 18. Spectral amplitudes of refracted waves at distances of 1·0 and 3·0 degrees for model in Fig. 15. Solid curve is spectrum for the interference head wave ($\beta_p = 5 \times 10^{-3}$ s^{-1}); dash-dotted curve is spectrum of diffraction head wave ($\beta_p = -5 \times 10^{-3}$ s^{-1}); dashed curve is spectrum for pure head wave.

Details of the scalloping associated with the exact numerical result for the interference head wave are illustrated in Fig. 13 for a homogeneous mantle and Fig. 17 for a mantle with a $5 \times 10^{-3}\ s^{-1}$ velocity gradient. Note that at small distances beyond the critical point, the interference head wave amplitudes are virtually coincident with the pure head wave amplitudes. With increasing distance, however, the scalloping increases and the relative amplitude levels of high frequency components gain with respect to those of lower frequency. Comparison of interference and pure head wave amplitudes in Fig. 13 suggests that the Earth's curvature has a significant effect on *Pn* amplitudes at distances as small as 2 to 3 degrees in the case of a homogeneous mantle.

The amplitude spectra for interference head waves at distances of 1·0 and 3·0 degrees are plotted in Fig. 14 for a homogeneous mantle and Fig. 18 for a mantle with a $5 \times 10^{-3}\ s^{-1}$ velocity gradient. The scalloped nature of these curves is characteristic of spectra for multiple, interfering wave forms. Note that the envelopes of the scalloped spectra fall off less rapidly with frequency than the spectral amplitude of the pure head wave.

Amplitude spectra for the diffraction head wave for a mantle with a $-5 \times 10^{-3}\ s^{-1}$ velocity gradient are also plotted in Fig. 18. These spectra are smooth and fall off more rapidly with frequency than the pure head wave as predicted by (20).

7. Conclusions

The above results emphasize Cerveny's (1966) observation that the pure head wave is a fragile entity. Its character is destroyed by small velocity gradients in the refracting medium as well as by slight curvature of the refracting boundary. The sensitivity of the closely-related diffraction and interference head waves to velocity gradients and boundary curvature, however, provide useful criteria for studying the fine velocity structure of the crust and upper mantle. Hill (1971a) used a simple application of these properties with published *Pg* and *Pn* amplitude data in an effort to infer some bounds on anelasticity and velocity gradients in the crust and mantle lid. Much more definitive applications should be possible, however, using the time series or spectra seismic waves recorded on broad-band digital instruments.

Acknowledgments

I should like to thank C. B. Archambeau for his advice and encouragement and P. G. Richards for many helpful discussions during this study. Much of the material presented in this paper is a result of doctoral research undertaken at the California Institute of Technology (Ph.D. Thesis, CIT). This research was supported in part by the Air Force Office of Scientific Research under Contract AFOSR F44620–69–C–0067.

National Center for Earthquake Research,
U.S. Geological Survey,
Menlo Park, California 94025.

References

Abramowitz, M. & Stegun, I. A., 1964. *Handbook of mathematical functions*, U.S. National Bureau of Standards.

Berry, L. A., 1964. Computation of Hankel functions, *U.S. National Bureau of Standards, Tech. Note* 216.

Berry, M. J. & West, G. F., 1966. Reflected and head wave amplitudes in a medium of several layers, *The Earth Beneath the Continents*, pp. 464–481, eds J. S. Steinhart and T. J. Smith, American Geophysical Union Geophysical Monograph 10, Washington D.C.

Brekhovskikh, L. M., 1960. *Waves in layered media*, Academic Press, New York, 561 pp.

Bremmer, H., 1949. *Terrestrial radio waves*, Elsevier, New York, 343 pp.

Buldyrev, V. S., 1964. Investigation of the Green's function for the problem of diffraction by a transparent cylinder with relative index of refraction less than one. Numerical methods for solving differential and integral equations and quadrature formulas, *Supplement to Zhurnal Vychislitel'noi Matematiki i Matematicheskoi Fiziki*, 4, Nauka.

Buldyrev, V. S. & Lanin, A. I., 1966a. Investigation of the Green's function for the problem of diffraction by a transparent cylinder, *Supplement to Zhurnal Vychislitel'noi Matematiki i Matematicheskoi Fiziki*, 1 Nauka.

Buldyrev, V. S. & Lanin, A. I., 1966b. Investigation of the interference wave field on the surface of an elastic sphere, in *Numerical Methods for the Solution of problems of Mathematical Physics* [in Russian], Nauka.

Bullen, K. E., 1963. *An introduction to the theory of seismology*, Cambridge University Press, London, 381 pp.

Cagniard, L., 1962. *Reflection and refraction of progressive seismic waves.* Translated and revised by E. A. Flinn and C. H. Dix, McGraw–Hill, New York, 282 pp.

Cerveny, V., 1965. The dynamic properties of reflected and head waves around the critical point, *Prace. Geofys. Ustavu. Cesk. Akad. Ved., Geofysikalni Sbornik*, pp. 135–245.

Cerveny, V., 1966. On dynamic properties of reflected and head waves in the *n*-layered Earth's crust, *Geophys. J. R. astr. Soc.*, **11**, 139–147.

Cerveny, V. & Jansky, J., 1967. On some dynamic properties of the diving wave, *Proc. of the 7th Assembly of the European Seismological Comm.*, pp. 397–402, Copenhagen.

Cerveny, V. & Ravindra, R., 1971. *Theory of seismic head waves*, Universtiy of Toronto Press, Toronto and Buffalo, 312 pp.

Chapman, C. H. & Phinney, R. A., 1972. Diffracted seismic signals and their numerical solution, *Methods in Computational Physics*, v. 12, *Seismology: Body Waves and Sources*, pp. 165–230, ed. B. A. Bolt, Academic Press, New York.

Chekin, B. L., 1964. On the reflection of elastic, spherical waves from an inhomogeneous half-space, *Izv. Geophys. Ser.*, No. 5, 711–717.

Chekin, B. S., 1965. The effect on a head wave of small inhomogeneities in a refracting medium, *Izv. Earth Physics Ser.*, **No. 3,** 1–10.

Fuchs, K., 1968. The reflection of spherical waves from transition zones with arbitrary depth-dependent elastic moduli and density, *J. Phys. Earth*, **16,** Special Issue, 27–41.

Gilbert, F. & Helmberger, D. V., 1971. Generalized ray theory for a layered sphere, *Geophys. J. R. astr. Soc.*, **27,** 57–80.

Grant, F. S. & West, G. F., 1965. *Interpretation theory in applied geophysics*, McGraw–Hill, New York, 584 pp.

Helmberger, D. V., 1968. The crust-mantle transition in the Bering Sea, *Bull. seism. Soc. Am.*, **58,** 179–214.

Hill, D. P., 1971a. Velocity gradients and anelasticity from crustal body wave amplitudes, *J. geophys. Res.*, **76,** 3309–3325.

Hill, D. P., 1971b. *High frequency wave propagation in the Earth: Theory and observation*, Ph.D. Thesis, California Institute of Technology, Pasadena.

Hill, D. P., 1972. An earth-flattening transformation for waves from a point source, *Bull. seism. Soc. Am.*, **62,** 1179–1194.

Hirasawa, T. & Berry, M. J., 1971. Reflected and head waves from a linear transition layer in a fluid medium, *Bull. seism. Soc. Am.*, **61,** 1–26.

Hoop de, A. T., 1960. A modification of Cagniard's method for solving seismic pulse problems, *Appl. Sci. Res. B.*, **8,** 349–356.

Jeffreys, H. & Lapwood, E. R., 1957. The reflexion of a pulse within a sphere, *Proc. Roy. Soc., London, Ser. A*, **241,** 455–479.

Knopoff, L. & Gilbert, J. F., 1959. Diffraction of elastic waves by the core of the Earth, *Bull. seism. Soc. Am.*, **31,** 694–705.

Langer, R. E., 1949. The asymptotic solutions of ordinary linear differential equations of the second order, with special reference to a turning point, *Trans. Am. Math. Soc.*, **67.**

Lanin, A. I., 1968. The calculation of interference waves for diffraction by a cylinder and a sphere, *Mathematical problems in the theory of propagation of waves*, pp. 27–44, ed. V. M. Babich, Leningrad, Nauka, Leningrad Div.

Merzer, A. M., 1971. Head waves from different transition layers, *Geophys. J. R. astr. Soc.*, **24,** 77–95.

Muller, G., 1970. Exact ray theory and the application to the reflection of elastic waves from vertically inhomogeneous media, *Geophys. J. R. astr. Soc.*, **21,** 261–283.

Muller, G., 1971. Approximate treatment of elastic body waves in media with spherical symmetry, *Geophys. J. R. astr. Soc.*, **23,** 435–449.

Nakamura, Y., 1964. Head waves from a linear transition layer in a liquid, *J. geophys. Res.*, **69,** 4349–4354.

Nussenzveig, H. M., 1965. High frequency scattering by an impenetrable sphere, *Ann. Phys.*, **34,** 23–95.

Phinney, R. A. & Cathles, L. M., 1969. Diffraction of *P* by the core: A study of long period amplitudes near the edge of the shadow, *J. geophys. Res.*, **74,** 1556–1574.

Richards, P. G., 1970. *A contribution to the theory of high frequency elastic waves, with applications to the shadow boundary of the Earth's core*, Ph.D. Thesis, California Institute of Technology, 278 pp.

Richards, P. G., 1971. Potentials for elastic displacement in spherically symmetric media, *J. acoust. Soc. Am.*, **50,** 188–197.

Scholte, J. G. J., 1956. On seismic waves in a spherical Eatrh, *Komnkl. Ned. Meterol. Inst. Publ.* 65.

Tolstoy, I., 1968. Phase changes and pulse deformation in acoustics, *J. acoust. Soc. Am.*, **44,** 675–684.

Appendix I

Evaluation of the poles of V_- for a subcritical gradient

Let the numerator and denominator of the reflection coefficient V_- (11a) be given by N_- and D_-, respectively. The Airy functions appearing in (11) are entire functions in the finite complex p-plane, and the only singularities of V_- will be associated with the zeros of D_-. In the region $|p-n_0| \ll 1$ (designated as $\mathscr{R}$) the term containing $Ai(-\zeta(p))$ dominates D_-, and the zeros of D_- will be near the zeros of $Ai(-\zeta(p))$. The argument of the Airy function in $\mathscr{R}$ is

$$-\tau(p) = -\zeta_0(p) \exp(i2\pi/3) \simeq -2n_0 \varepsilon^{-2}(n_0-p) \exp(i2\pi/3). \qquad \text{(A1.1)}$$

A simple application of the Newton–Raphson algorithm shows that the zeros of D_- are approximately given by

$$p_j \simeq n_0 + \frac{\varepsilon^2 a_j}{2n_0} \exp(i\pi/3), \tag{A1.2}$$

where a_j is a real, positive number defining the j-th zero of $Ai(-a_j)$ (see Table 10.13 in Abramowitz & Stegun 1964).

The residues of (14) with V_- in the integrand are given by

$$\text{Res} = \left\{\frac{\sqrt{p}}{q}\frac{N_-}{D_-'}\frac{d\zeta}{dp}\exp(i\phi)\right\}_{\zeta=a_j}, \tag{A1.3}$$

where

$$\phi = k_0 R_1(qq_0 + pp_0)$$

$$q(\zeta) \simeq q_c - \frac{\varepsilon^2 \tau \exp(i\pi/3)}{2q_c}; \quad q_c = (1-n_0^2)^{1/2}.$$

For $\varepsilon^2 q_c \ll |m^2 q|$

$$\left\{\frac{\sqrt{p}}{q}\frac{N_-}{D_-'}\frac{d\zeta}{dp}\right\} \simeq -\frac{i\varepsilon^3}{\sqrt{(n_0)}q_c^2 m}$$

and (A1.3) becomes

$$\text{Res} \simeq -\frac{i\varepsilon^3}{mn_0^{1/2}q_c^2}\exp\left[i\left(\phi_0 + \frac{k_0 L\varepsilon^2 a_j \exp(i\pi/3)}{2n_0}\right)\right] \tag{A1.4}$$

which leads directly to (17) in Section 5.1.

Appendix II

Evaluation of the poles of V_+ for a supercritical velocity gradient

The analysis for this case parallels that given in Appendix I for the subcritical velocity gradient except that here it is necessary to carry an extra term in the expansions about $p = n_0$ to insure that the residue series converges. In this case let the numerator and denominator of V_+ be given by N_+ and D_+, respectively. As before, the term containing $Ai(-\zeta_0)$ dominates D_+ in $\mathscr{R}$ and the zeros of D_+ approximately given by

$$p_j = \left(n_0 - \frac{\varepsilon^2}{2n_0}a_j\right) + i\frac{\varepsilon}{q_c m}\left(1 + \frac{\varepsilon^4 a_j}{n_0^3}\right). \tag{A2.1}$$

The residues of (14) with V_+ in the integrand are given by (A1.3) with N_+, D_+' and ζ_0 in place of N_-, D_-' and τ. In this case, however

$$\left\{\frac{\sqrt{p}}{q}\frac{N_+}{D_+'}\frac{d_0}{d_p}\exp(i\phi)\right\}_{\zeta_0=a_j} \simeq \frac{i\varepsilon^3}{\sqrt{(n_0)}q_c^2 m} \tag{A2.2}$$

$$p \simeq n_0 - \frac{\varepsilon^2\zeta_0}{2n_0} - \frac{\varepsilon^4\zeta_0^2}{8n_0^2}$$

$$q \simeq q_c + \frac{\varepsilon^2\zeta_0}{2q_c} - \frac{\varepsilon^4\zeta_0^2}{8q_0}$$

and

$$\phi = \phi_0 - \frac{k_0 L\varepsilon^3}{2n_0 q_c m} - i\frac{k_0 \varepsilon^2}{2n_0}\left[\left(L - \frac{iL^*\varepsilon^3}{{n_0}^2 q_0 m}\right) a_j + \frac{\varepsilon^2 L^*}{2{n_0}^2} {a_j}^2\right].$$

Substituting these results into the expression for the residues (A1.3) leads directly to (22) in Section 5.2.

List of principal symbols

Symbol	Meaning	Equation or Figure
a	Radius of inhomogeneous sphere	3
a_j	j-th zero of $A_i(-\tau)$	16
A_i, A_i'	Airy functions	10
$\mathscr{A}^{(1)}, \mathscr{A}^{(2)}$	Airy function ratios	26
c, c_0, c_s	Acoustic wave velocity	4, 6
d, d_0	Density	9
k, k_0	Wave number	3
L, L_s, L_r	Path lengths of the critical ray	Fig. 2
L_d	Horizontal distance covered by diving ray	Fig. 9
L^*	Distance parameter	22
l	Spheroidal order number	3
m	Density ratio	11
n_0	Index of refraction	6
p	$\sin\theta$	10
p_0, p_n	Saddle points for reflected wave and diving waves	Fig. 4(b) Fig. 6
P	Deviation from ambient acoustic pressure	1
q, q_0	$\cos\theta, \cos\theta_0$	10
q_c	$\cos\theta_c = \sqrt{(1-{n_0}^2)}$	22
r	Radius in spherical co-ordinates	3
R_1	Path length of refracted ray	Fig. 2
V_s	Spherical reflection coefficient	3
$V_\pm$	Plane wave reflection coefficient for $\delta < 0$ (−), $\delta > 0$ (+)	11
V_0	Plane wave reflection coefficient for two homogeneous half spaces	12
Y_0, Y_n	Factors in generalized ray expansion of V_+	26
z, z_0	Elevation of receiver and source	3
z_{min}	Minimum bottoming depth for ray description of diving wave	31
β, β_p	Velocity gradients	8
γ, γ_p	Index of refraction gradients	6
ε	Dimensionless gradient parameter	11

ζ, ζ_0	Airy function arguments	11
η	Radial component of k	3
Θ	Spherical co-ordinate	3
θ, θ_0	Angle of incidence	Fig. 2
θ_c	Critical angle of incidence	Fig. 2
κ	Angular component of k	3
ρ	Arc distance along boundary	3
ρ_c	Critical arc distance	22
ρ^*	$a \sin(\theta)$	14
$\rho_{\min}$	Minimum distance for ray description of diving wave	32
σ_-, σ_+	Dimensionless parameter in asymptotic solutions	18, 23
Φ	Acoustic pressure potential	1
Φ_{r-}, Φ_{r+}	Reflected wave potential $\gamma < 0$, $\gamma > 0$	15, 28
Φ_{h-}	Diffraction head wave potential	20
Φ_{h+}	Interference head wave potential	24
$\Phi_d^{(n)}$	n-th diving wave potential	30
ϕ_0	Pure head wave phase	17